Pneumatic Power Regulation by Wave Forecasting and Real-Time Relief Valve Control for an OWC

Pneumatic Power Regulation by Wave Forecasting and Real-Time Relief Valve Control for an OWC

Kieran Monk[#*1], Daniel Conley[#2], Miguel Lopes[*3], Qingping Zou[+4]

[#]*School of Marine Science and Engineering, University of Plymouth Plymouth, PL48AA, UK*
[1]kieran.monk@plymouth.ac.uk
[2]daniel.conley@plymouth.ac.uk

[*]*WAVEC offshore renewables Lisbon, 1400-119, Portugal*
[1]kieran@wavec.org
[3]mlopes@wavec.org

[+]*Department of Civil and Environmental Engineering, University of Maine Orono,ME 04469, USA*
[4]qingping.zou@maine.edu

***Abstract*— The shore mounted "Pico" OWC has a relief valve mounted in parallel to the turbine which connects the chamber to the atmosphere. The aperture of this valve is adjustable and can be used to regulate the pneumatic power exposed to the turbine. Here we develop an algorithm to actively control the relief valve aperture so that the peak pneumatic power of each wave cycle approaches but does not breach the turbine stall threshold, thus providing the maximum pneumatic power possible without the turbine stalling. The relief valve aperture is slow to adjust so the hydrodynamic and pneumatic behaviour is forecasted to allow enough time to achieve the correct aperture before the wave reaches the chamber. The chamber hydrodynamics are forecasted using a neural network that considers hydrodynamic measurements made 60 meters up wave and other operational, environmental and preceding wave, parameters. Turbine stalls were identified approximately by the gradient in turbine vibration and the angular velocity dependent pneumatic power threshold for turbine stall is found empirically. The relationship between the forecasted chamber hydrodynamics, relief valve aperture and the resultant pneumatic behaviour, is also found empirically and this is used to select the relief valve aperture that the control algorithm targets.**

***Keywords*— OWC, control, forecasting, wave energy, Pico, relief valve, artificial neural network**

I. INTRODUCTION

Pico is one of the few full scale, grid connected, wave energy converters (WEC) in the world. It is a shore mounted oscillating water column type WEC located on the Portuguese island of Pico in the Azores archipelago. The plant has a chamber with a submerged opening to incident waves. Details and dimensions of the plant can be found in [1]. The oscillation of the water surface from wave action acts as a piston to compress and expand air in the chamber, creating a reciprocating flow through a duct connected to the atmosphere that house a Wells turbine connected to a generator. A Wells turbine is used because the tangential lifting force on the turbine blades is in the same direction regardless of the air flow direction. Also the comparative simplicity of a fixed blade turbine compared to variable pitch turbines is appealing. However, one limitation of the Wells turbine is the stall effect. The angle of attack of the turbine blades is the angle between the vector sum of both the velocity of the blades and the velocity of the driving air flow, and the plane of the turbines rotation. When the turbines velocity slows or the driving airflow velocity increases the angle of attack increases. At a critical upper threshold of the angle of attack, the boundary layer separates from the blade surface leading to a loss of lift and increased drag. When this occurs the turbine is classified as stalling. The pneumatic to mechanical power conversion efficiency is also dependent on the relative angle of attack and the stall effect limits the upper level of pneumatic to mechanical power transfer. When the turbine is stalling high levels of vibration and noise occurs, which has both significant: accelerated mechanical fatigue and environmental impact, implications.

To extend the operational sea-state range of the plant, a large slow moving sluice gate, acting as a pressure relief valve, is installed in parallel to the turbine, on the roof of the chamber as shown in Fig.1. The aperture of the relief valve when fully opened measures 1.3m by 1.3m. It is actuated by a hydraulic ram and takes approximately 26 seconds to move its full range. This can be partially or fully closed to regulate the pneumatic power exposed to the turbine, and to vent over pressure from the chamber when the plant is not operational. This allows the machine to operate in a much broader range of sea states without the frequency and intensity of stalls becoming unacceptably high. Without the relief valve the operational range would be quite limited.

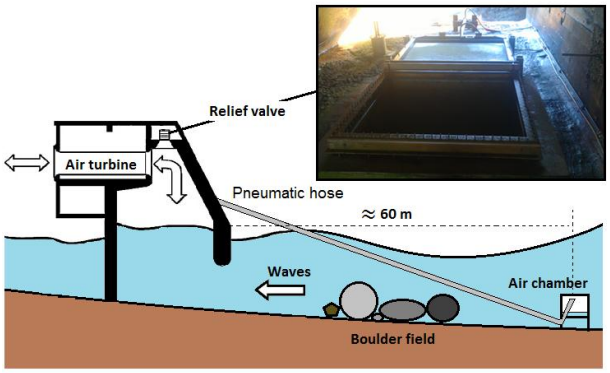

Fig. 1 Cross shore schematic of the OWC plant and near-shore sensor system (air-chamber). The location of the relief valve is shown along with a picture of the actual valve.

Previously the relief valve aperture control was done in an essentially static way and was only adjusted when the sea state

changed significantly. The stall effect was a frequent occurrence, but only for the peak flow of the exhale (compression) part of compression/expansion cycle. Besides selecting different power take off curves, operational control was limited to either: setting a smaller relief valve aperture which would deliver more pneumatic power to the turbine with greater levels of power production generally being achieved, but incurring more frequent stalls of the turbine, or with a greater valve aperture wasting more pneumatic to the atmosphere but incurring less frequent stall events.

Two types of control strategies have been identified to maximise power generation and/or minimising turbine stall frequency: 1.) control the electromagnetic torque applied to the turbine and 2.) control chamber pressure with a relief valve. These control strategies may be used independently or simultaneously.

As discussed extensively in [2] and [3] the electromagnetic torque imposed on the turbine by the generator can be controlled to better match the turbine speed to the available wave energy in order to enhance the power production and/or reduce the frequency of turbine stalls. Active electromagnetic torque control could be used on a wave by wave basis using short term forecasting to provide sufficient time for the adjustment of the turbines angular velocity. Alternatively different angular velocity dependent power take off curves can be defined for different sea states which aim to keep the turbines rotation speed in a range that is most receptive to the greatest proportion of waves for the that particular sea state.

Regulating the chamber pressure with relief valve control is theoretically considered in [4]. A series of hypothetical fast acting relief valves (around 0.07s for full aperture change) which actuate based on real-time pressure readings in chamber with a small delay (which is varied and assessed in the study). The combined total aperture of the series of relief valves was $1m^2$. The control system is simulated numerically with the relevant physical, operational, and wave climate, parameters of the Pico OWC. In [4] the potential increase in annual power production from this hypocritical relief valve configuration and control strategy is assessed and found to be around 25%.

In this study we concentrate on the developing a control strategy to regulate the pneumatic power exposed to the turbine by adjusting the relief aperture in real-time. This relief valve control strategy necessarily differs significantly from the hypothetical control strategy and relief valve configuration presented in [4]. This is because the actual relief valve installed at the Pico OWC has a slow aperture adjustment rate. As such rapid response of the valve to the evolving pressure measured in real time in the chamber is not possible and forecasting of the hydrodynamics in the chamber is required to provide enough time to sufficiently adjust the relief valve aperture. Control with electromagnetic torque is not considered.

In the literature two main options exist for short-term wave forecasting for wave by wave control of a WEC. The first is to forecast the hydrodynamics at the WEC using past measurements also made at the WEC. In [5] the ability of a number of forecast models to predict the surface elevation at a wave buoy from previous data is assessed. The best results were achieved with an autoregressive model giving good accuracy within a prediction horizon of up to 2 wave periods in advance. In [6] adaptive filters are used for short-term wave prediction and are implemented into a programmable logical controller to assess the actual functionality in real-time. The prediction horizon for an accurate surface elevation forecast was much shorter than in [5] which was only a couple of seconds, although wave period was forecasted well at longer prediction horizons. The second option for short-term wave forecasting is the prediction of the incident wave parameters at the WEC from measurements made up wave of the WEC. This is considered in [7], [8] using filtering methods and in [9] using wave propagation modelling.

In this study we opted to use a neural network to forecast the chamber hydrodynamics from measurements made approximately 60m up-wave of the chamber front wall. The forecast model and control algorithm is discussed in more detail in the following methods section.

II. Methodology and Results

Originally an "Aquadopp" combined hydrostatic pressure sensor and ADCM (acoustic Doppler current meter) unit was used to measure and record the hydrodynamics approximately 60m up wave of the chamber front wall. Due to the extremely harsh wave climate the data cable providing the live data was severed almost immediately by boulder movement. The Aquadopp was repeatedly re-deployed to record data internally but the live data was not available. Due to the expense of the cable and the likelihood of repeat damage an alternative system to measure the incident wave hydrodynamics was developed and deployed at the same location as the ADCM in spring 2012. The system is a hydrostatic wave pressure sensor. A small steel box with an open bottom edge is periodically filled with air from a compressor inside the plant via a pneumatic hose supported by a steel cable. A basic schematic of the setup is given in Fig. 1. The pressure of this trapped air pocket is then measured in the plant with a pneumatic pressure transducer via the same pneumatic hose. The water surface elevation is then estimated by;

$$\eta_{ns} \approx p_h/\rho g \quad (1)$$

where p_h is the hydrostatic water pressure approximately 60m in front of the chamber wall, ρ_w is the density of sea water, g is the acceleration of gravity. It is an estimate of vertical surface velocity because some hydrodynamic or pneumatic losses might occur. From here forward we will refer to any

measurements made at the pneumatic or Aquadopp sensors, which are both located approximately 60 meters in front of the chamber wall, as “near-shore” measurements.

The near-shore sensor provides measurements of the incident wave hydrodynamics, which after: electrical, media conversation and computational processing delays, gives approximately 7 seconds before the same part of the wave cycle occurs in the chamber. The relief valve aperture can be adjusted by approximately 30% of its full range in 7 seconds which allowed real-time active control of the relief valve to be considered for the first time. A simple algorithm was deployed to control the relief valve using the estimated vertical water surface velocity $\dot{\eta}_{ns}$ measured at the near-shore sensor as an indicator of the subsequent hydrodynamics in the chamber and the potential for this to result in a turbine stall. It relied on a few basic logical commands and recorded the response which it used to self-adapt its operational parameters. Its self-adaptation objective was to find an optimal equilibrium state, where the mean relief valve aperture was as small as possible whilst the frequency of turbine stalls and relief valve actuation cycles did not exceed the number defined by the operator. This equilibrium state was constantly being evaluated and would change with the changing sea state. The function of the control system was to evaluate each incident wave and to open the relief valve aperture on the detection of substantially larger waves to exhaust excessive pressure. A more closed relief valve aperture would be set for the lulls between periods of strong wave action.

Despite the simplicity of the system, turbine stalls were reduced to a very low frequency. This first active relief valve control system was only operational in its final form for a total of 4 days before the Pico plant entered an extended non-operational period. Therefore, it is not possible to make rigorous quantifications of the changes in power production. However, during this short period a 15 minute mean power production of $68kW$ was achieved surpassing the old record of $65kW$. This initial indication of enhanced power production is supported when we assess the power matrices with and without the control algorithm as shown in Fig. 2. The data points of Fig. 2 show the maximum mean production achieved in any 15 minute period for (a) all available data preceding the relief valve control system deployment and (b) the 4 days with the relief valve control system functioning. The average enhancement of power production over all sea sates is seen to be 5% when using the relief valve control system. The data pool for relief valve control is low and the result is not conclusive. However, the comparison is considered to be as harsh as possible in evaluating any potential improvements in power production from relief valve control. This is because we are comparing the maximum production values over a 2 year period (without relief valve control) against 4 days (with relief valve control).

The original relief valve control system has much room for improvement because it did not factor many of the variables that are theoretically important in forecasting the transmission of incident wave hydrodynamics from the near-shore to the chamber, and the resultant pneumatic power delivered to the turbine.

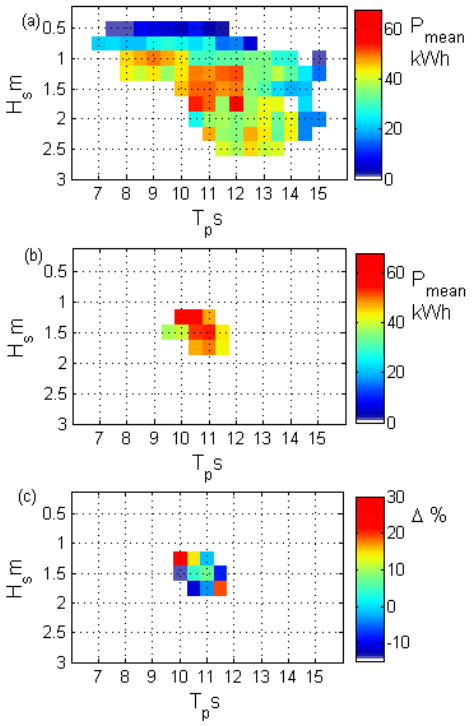

Fig. 2 Comparison of the power matrices for maximum mean power in any 15 minute period for different permutations of significant wave height H_s and peak period T_p using all available data, for: (a) without relief valve control, (b) with relief valve control and (c) the difference between no relief valve control and relief valve control as a percentage of the corresponding no relief valve control maximum power value.

The objective of this research is to develop a new algorithm to actively control the relief valve aperture so that the peak pneumatic power of each wave cycle approaches but does not breach the turbine stall threshold, thus providing the maximum pneumatic power possible, considering the limitations of the actual relief valve installed at Pico, without the turbine stalling. Adjustment of the relief valve is slow so short-term forecasting of the hydrodynamic transfer from the near-shore to the chamber and the resultant pneumatic behaviour is required to allow sufficient time to set the relief valve aperture, before the incident wave reaches the chamber.

Forecasting the optimal relief valve aperture from incident near-shore wave measurement was achieved in three distinct steps: 1.) Forecast the hydrodynamics in the chamber from the measured hydrodynamics at the near–shore sensor. 2.) Determine the threshold angular velocity dependent maximum air-velocity that the turbine can be exposed to without a stall occurring. 3.) Predict the optimum relief valve aperture that delivers the maximum air velocity to the turbine without breaching the angular velocity dependent stall threshold (step 2), from the forecasted chamber hydrodynamics (step 1).

As we are in the rare position of having operational data at our disposal, we opted to derive the forecast stages from the data instead of from theory. The main motivation for this is that the basic theory for hydrodynamic transfer, hydrodynamic to pneumatic transfer and mechanical response, might not factor in the specifics of the Pico plant. These include but are not limited to: hydrodynamic and pneumatic losses in the chamber and duct system due to the large holes that have developed, the specific shape of the coastline and its effect on wave reflections effecting the near-shore wave measurements, the exact location, type, limitations and noise in the sensor and data acquisition systems used. It should be noted at this point that as the control algorithm will ultimately operate with sensor data in real-time the forecast stages were derived from existing data that was only filtered in a way that can be replicated in real-time i.e. box car averages etc. All forecast stages are deterministic.

A. Forecast step 1 – The vertical water surface velocity in the chamber

In order to forecast the pneumatic power exposed to the turbine we first need to forecast the vertical water surface velocity $\dot{\eta}_c$ (time derivative of surface elevation) in the chamber, as this controls the rate of air compression. For convenience we will sometimes refer to the vertical water surface velocity in the chamber $\dot{\eta}_c$, normalised by the vertical water surface velocity at the near-shore sensor $\dot{\eta}_{ns}$. The ratio $\dot{\eta}_c/\dot{\eta}_{ns}$ is similar to the amplification factor or RAO (response amplitude operator) parameter commonly used in the literature which refers to the normalised surface elevation.

As discussed earlier the forecast stages and control algorithm were developed using operational data. To achieve forecast step. 1 we used an Artificial Neural Networks (ANN), because of its ability to finding complex relationships in data involving a large number of variables. For the ANN to find patterns between known input data and target data, and therefore be effective in forecasting an unknown output from future input data, it must be provided with the relevant physical parameters that influences the output. Therefore, even though we will not use theoretical relationships directly to construct our forecast system, it is still important to review the literature to identify which variables could be important, and ensure this data, where possible, is available to train the ANN. In the literature we see that $\dot{\eta}_c/\dot{\eta}_{ns}$ is theoretically dependent on a number of variables which are identified in the following.

The water mass oscillating in the chamber will have a natural frequency. The resonant wave period T_n is given in [10] as

$$T_n = 2\pi\sqrt{l/g} \tag{2}$$

where l is the water column draft in the chamber and g is gravitational acceleration constant. This is modified in [11], to account for water columns of large horizontal cross-sectional area S;

$$T_n = 2\pi\sqrt{(l + 0.41S^{0.5})/g} \tag{3}$$

Both the incident wave period and tide position (which effects the water column draft l) will theoretically affect $\dot{\eta}_c/\dot{\eta}_{ns}$ because of resonant amplification and should be included in the training of the ANN. The maximum tidal range at the Pico plant is 1.8m.

As shown experimentally in [12] and numerically in [13], when the hydrodynamic flow rate at the chamber lip, from the volume flux of water entering the chamber from wave action, is high enough, separation of flow occurs. Under these conditions vortices are formed that dissipate energy and reduce the hydrodynamic transfer efficiency. By continuity the hydrodynamic flow rate at the chamber lip is dependent on the vertical velocity of the water surface in the chamber $\dot{\eta}_c$. As $\dot{\eta}_c$ is a function of the amplitude of the incident wave and also the wave period, both because of amplification through resonance (equation 2) and simply because of the angular velocity, both incident wave amplitude and wave period (already identified) will theoretically affect the hydrodynamic efficiency and consequently $\dot{\eta}_c/\dot{\eta}_{ns}$ and should be both included in the training of the ANN.

The chamber lip is further investigated in [14] who show experimentally that when the gap between the sea floor and the chamber lip is shorter, the hydrodynamic flow rate into the chamber must be greater for continuity. Therefore separation of flow occurs for smaller $\dot{\eta}_c$ with associated reduction in hydrodynamic efficiency. However this effect was found to be negligible past a certain threshold of $\dot{\eta}_c$ because separation of flow appears to approach an upper limit so that the hydrodynamic losses are somewhat limiting. They also confirm the relationship in equation 2, that the resonant period is shifted to a larger value when the draft of the front wall is greater because the increased mass confined in the chamber changes the natural frequency. The chamber horizontal cross sectional area is 12m x 12m, the thickness of the front wall is 1.8m and has a draft of 2.5m from mean water level and has a semi-circular lip.

As shown in [15], using a boundary element model, the length of the chamber also effects the amplification of incident waves in the chamber and the resonant period. However in the case of the Pico OWC the chamber length is constant so data specific to this cannot be given to the ANN to construct the forecast matrix for forecasting $\dot{\eta}_c$, but this effect will be included indirectly in the result.

The consideration of the compressibility of air in the chamber and damping is shown in [16] to shift the optimum performance period to a lower value than described by just the dimensions of the plant and the oscillating water column mass (when air is considered incompressible). Therefore, air compressibility can either amplify or dampen the oscillation of the water column in the chamber depending on the incident wave period. They assess the effect of the non-dimensional air compliance parameter, α/μ, on the power capture;

$$\frac{\alpha}{\mu} = \frac{\rho_w g h}{\gamma p}\left(1 - \frac{{T_n}^2}{T^2}\right) \quad (4)$$

where h is the effective height of the air chamber (air-chamber volume / water surface area), T is the incident wave period, ρ_w is the density of water and γ is the specific heat capacity of air, and ρ_0 the density of air at atmospheric pressure. They find that the air compressibility acts to decrease the device's power capture performance when $0 < \alpha/\mu$. The peak performance maxima is found at a point when $0 > \alpha/\mu$, which exceeds that of when air compressibility is not considered.

In [16] the compressibility of air is also seen to affect the power capture and this is a function of the volume of the air chamber which again is a function of the tidal position.

The mass flow rate of air leaving from the relief valve will affect the pressure evolution in the chamber and hence the radiation wave damping effect, on the hydrodynamic efficiency, which is potentially significant as shown in [13]. The mass air flow rate from the relief valve (for an ideal gas with flow being an isentropic process) is given in [17] as;

$$\dot{m}_v = k_v sgn(p^* - 1)[2p_0\rho_0 {C_d}^2 {A_v}^2 {p^*}^{\frac{1}{\gamma}}|p^* - 1|]^{0.5} \quad (5)$$

where k_v is the valve aperture (0 for closed and 1 for open), A_v the aperture area, C_d the discharge coefficient, and γ the isentropic expansion factor.

As shown in [17] the mass flow rate of air $\dot{m}$ passing the turbine is dependent on the angular velocity N;

$$\dot{m} = Dp_0(p^* - 1)/Nk_1 \quad (6)$$

where D is the turbine diameter, p_0 is the atmospheric pressure, $p^* = p/p_0$, where p_c is the chamber pressure and $k_1 = \Psi/\Phi$ which is the dimensionless turbine characteristic, with $\Psi = p_c/p_0 N^2 D^2$ being the pressure coefficient and $\Phi = \dot{m}/p_0 ND^3$, the flow coefficient. As the angular velocity of the turbine regulates the rate at which air can escape the chamber it will also influence the damping effect from the compressed air in the chamber, as discussed previously. Therefore. the turbine angular velocity should also be provided in the construction of the ANN which is used to form the forecast matrix. However, this will likely be eclipsed by the effect of the relief valve position which could not be included in the formation of ANN at this point in time due to insufficient data.

Unfortunately the acquisition of data for the relief valve position only commenced a short while before the Pico plant last operated and operational data with the relief valve position recorded is too limited to be included in the construction of the ANN. To factor in the effect of chamber pressure on wave radiation and the effect this has on damping oscillation and hence the forecast $\dot{\eta}_c/\dot{\eta}_{ns}$, we would also need to be able to forecast the chamber pressure associated with the incident wave measured at the near-shore sensor. Measuring it in real-time, of course, would be too late to be factored in to the relief valve control. As the effect of the relief valve position will have such a large effect on the evolution of the chamber pressure, it does not seem appropriate to attempt to forecast chamber pressure and include this forecasted variable in the training data for the ANN, without first having information on the relief valve position. Addressing this issue will hopefully further enhance the forecast in the future when sufficient data becomes available.

Finally, as the control algorithm will rely heavily on the incident wave parameters measured at the near-shore sensor, interference from wave reflections is a major consideration and potentially a limiting factor. Depending on the amplitude and period of the preceding wave (reflected from the plant), and incident wave constructive or destructive interference will occur to some extent modifying the measurement of the true incident wave parameters at the near-shore sensor. Therefore, we provide the ANN with information regarding the preceding wave from both the near-sensor and the chamber. So that any relationship between preceding waves (reflected from the plant) and the subsequent modification of the incident wave's parameters due to interference, will be factored into the forecast.

To construct the ANN for forecasting the vertical water surface velocity inside the chamber, the following parameters as identified in the above to theoretically influence the $\dot{\eta}_c/\dot{\eta}_{ns}$, and that would be available in real-time to the final control algorithm, were provided in the training of the ANN;

1. The zero up crossing wave period measured 60m in front of the plant T_{ns}
2. The preceding zero up crossing wave period measured 60m in front of the plant T_{ns-1}
3. The preceding zero up crossing wave period measured in the chamber T_{c-1}
4. Peak water surface vertical velocity measured 60m in front of chamber $\dot{\eta}_{ns}$
5. Preceding Peak water surface vertical velocity measured 60m in front of chamber $\dot{\eta}_{ns-1}$
6. Preceding peak water surface vertical velocity measured in chamber $\dot{\eta}_{c-1}$
7. Tidal displacement from mean water level
8. Turbine angular velocity ω_T

Because the relief valve is slow moving, synchronisation of the relief valve aperture to the full cycle of $\dot{\eta}_c$, is not possible. Therefore, our relief valve control strategy is limited to a single relief valve aperture size per wave cycle. As the primary goal of this research was to maximise pneumatic power delivery to the turbine, whilst eliminating stalls, this target aperture size will be such that the peak positive value of $\dot{\eta}_c$ of the wave cycle delivers a level of pneumatic power to the turbine that is close to but does not breech the threshold for stall. As such the peak value of $\dot{\eta}_c$ is the ANN forecast target, and a full time-series prediction of $\dot{\eta}_c$ is of little use. If in the future a faster acting relief valve is installed that could

keep pace with the change in $\dot{\eta}_c$, throughout the entire wave cycle, a forecast of the full time-series of the water surface vertical velocity in the chamber would be desirable. This would result in an ideal situation where the maximum tolerable and available, pneumatic power is delivered to the turbine throughout the full wave cycle and not just at the peak of the exhale part of the cycle. A forecast of the full time-series of $\dot{\eta}_c$would require the application of a dynamic neural network due to the time lags in dynamics of the system.

For our purposes, a simple feed forward ANN is sufficient for generalisation between the input data vector (containing the relevant parameters of a full wave cycle) and the output peak $\dot{\eta}_c$. The network was constructed with one hidden layer containing 10 neurons as this was found to give marginally greater accuracy than with other numbers of neurons that we tested. The network was trained using the Lavenberg-Marquardt back-propagation learning algorithm. 52000 independent data vectors, each representing one completed wave cycle (as defined by the zero up-crossing at the near-shore sensor) were used to: train, validate and test the network. being randomly divided into the following proportions: 70%, 15% and 15%, respectively.

Although we do not instruct the ANN on the dependency strength of the output on each input variable, it is still interesting to analyse the dependency of the target $\dot{\eta}_c$ on the different individual input variables. This is most easily interpreted when $\dot{\eta}_c$ is normalised by $\dot{\eta}_{ns}$. As $\dot{\eta}_c/\dot{\eta}_{ns}$ is dependent on many factors simultaneously and because of noise and fluctuations in the data quality, the data points of $\dot{\eta}_c/\dot{\eta}_{ns}$ with respect to a single variable are distributed broadly. In order to identify any underlying trends we must apply some sort of fitting curve. A polynomial of degree 5 was chosen to show the best fit trend line for each variable and these are seen in Fig. 3. Three data periods corresponding to three complete deployments and data retrieval of the Aquadopp hydrostatic pressure sensor were used to assess the relationships between $\dot{\eta}_c/\dot{\eta}_{ns}$ and the different variables considered. The data from the three periods are kept separate in order to confirm that any trend lines fitted with the polynomial are consistent in both scale and shape throughout the data.

There are a number of interesting points to note from the subplots of Fig. 3. Fig. 3a shows that the profile $\dot{\eta}_c/\dot{\eta}_{ns}$ with respect to $T_{ns}$is skewed compared to what we expect from the theory in [18] for example. The natural period appears to be 15s which is significantly higher than the dominant wave period for this geographic location that the plant's dimensions where designed for, which is in the region of 11s. Also there appears to be a second resonant peak at very short wave periods.

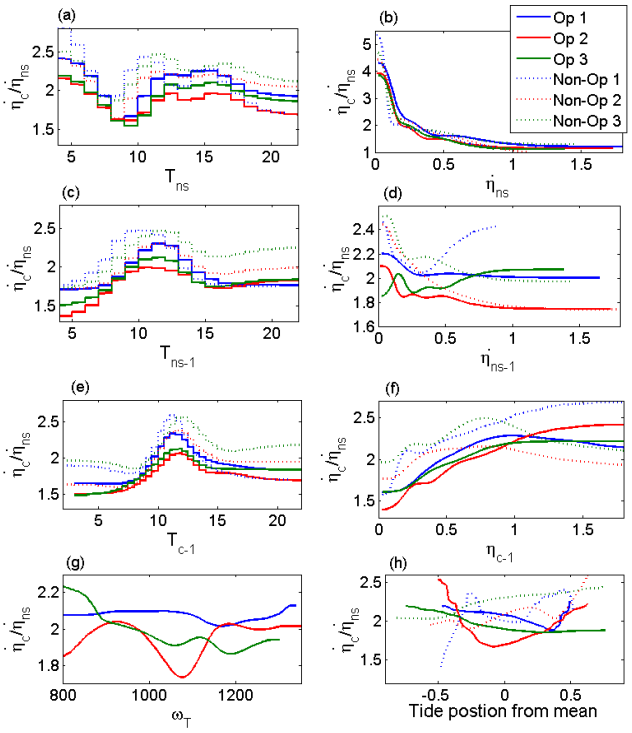

Fig. 3 Polynomial fitted curves of order 5, fitted to raw data corresponding to three Aquadopp deployment periods 1.) blue - 08/11/2010 – 21/11/2010, 2.) red - 21/11/2010 – 22/02/2011 and .3) green - 21/02/2012-22/03/2012, showing the relationship $\dot{\eta}_c/\dot{\eta}_{ns}$ when the plant is both operational and non-operational for the following parameters; (a) zero-up crossing wave period (near-shore), (b) water surface vertical velocity (near-shore), (c) preceding zero-up crossing wave period (near-shore), (d) preceding water surface vertical velocity (near-shore), (e) preceding zero-up crossing wave period (chamber), (f) preceding water surface vertical velocity (chamber), (g) turbine angular velocity, (g) tide position from mean.

The wave period spectral distribution, given in Fig. 4a, shows a significantly higher number of shorter period waves recorded at the near-shore sensor compared with to those recorded at the chamber. This strongly suggests that waves reflected from the plant structure and surrounding coastline interfere with incident waves at the near-shore sensor, causing artificial zero crossings to be registered so that a longer period wave is registered as becomes two short period waves.. This is affirmed by examining the difference in wave period of each wave as it is measured at the near-shore sensor and subsequently in the chamber as shown in Fig. 4b. A greater proportion of waves have a shorter wave period measured at the near-shore sensor than in the chamber showing that in terms of zero crossings and wave period measurements, destructive interference dominants the shift in wave period distribution. Constructive interference is also present as seen by the proportion of waves that have their wave period extended. The artificial down crossing from destructive interference will result in waves which appear to have very short wave periods but that also have the amplification of longer waves (in the chamber). This would explain the apparent resonant peak seen for short wave periods in Fig 3a, that does not agree with the theory.

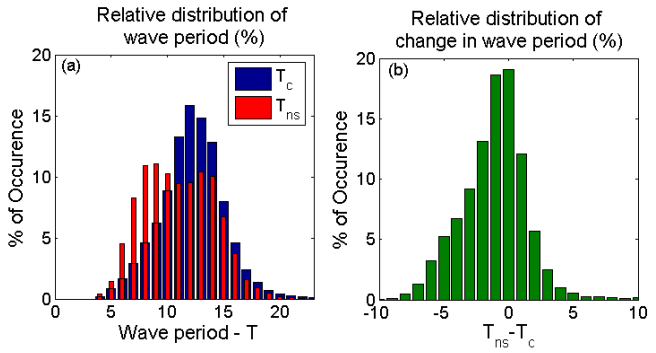

Fig. 4 (a) Comparison of wave period spectral distribution of wave periods as measured in the chamber with the wave period measured at the near-shore sensor. (b) The difference in wave period measured at the near-shore sensor and the wave period measured for the same wave in the chamber. Plots are histograms are shown as percentages of the total the sample size which is 52000 completed wave cycles.

Fig. 3b again shows the effect of destructive interference, as there is a relatively large value of $\dot{\eta}_c/\dot{\eta}_{ns}$ when $\dot{\eta}_{ns}$ is small. But again this is likely an artefact as in actuality the incident wave has been destructively interfered with at the near-shore sensor location rather than being amplified to such large extents by resonance in the chamber. It may however be enhanced by the low viscous losses associated with low hydrodynamic flow rates for smaller waves. There is also a steady decline in $\dot{\eta}_c/\dot{\eta}_{ns}$ with increased $\dot{\eta}_{ns}$ which could be explained by increased hydrodynamic viscous losses and/or from radiation damping from the increase in chamber pressure assorted with larger waves. Fig 3c shows the preceding wave amplification curve which is more in line with what we would expect Fig. 3a to look like from the theory (if there were no reflected waves) with a clear natural period peak. Fig. 3d shows there is no clear relationship between the preceding wave's vertical surface velocity at the near-shore sensor and $\dot{\eta}_c/\dot{\eta}_{ns}$. This is likely to be because some preceding waves are smaller and some larger and overall they cancel each other out when the polynomial curve is fitted, leaving a mean amplification factor of approximately 2.

Fig. 3e shows the relationship between $\dot{\eta}_c/\dot{\eta}_{ns}$, and the preceding wave period as measured in the chamber. As the preceding wave is likely to have a wave period similar to the incident wave, the resonance curve takes the form of what we expect from the theory (see for example [18]). One residual difference from the theory is the grater amplification of very short period waves which again might be explained by destructive interference at the near-shore sensor. Fig. 3f shows that $\dot{\eta}_c/\dot{\eta}_{ns}$ is greater when $\dot{\eta}_{c-1}$ is greater, the only possible explanation we were able to make for this is that reflected preceding waves of greater $\dot{\eta}$ would interfere more strongly with the incident wave, which as show in Fig. 3b, is most likely to be in the destructive direction, resulting in a greater value of $\dot{\eta}_c/\dot{\eta}_{ns}$.

Fig. 3g shows that there is no clear relationship between $\dot{\eta}_c/\dot{\eta}_{ns}$ and the turbine angular velocity ω_T. This is likely to be because the relief valve aperture is not considered and would likely eclipse the effect on the pressure evolution from the regulation of airflow by the turbines angular velocity (equation 6). From the theory we might expect to see a reduction in $\dot{\eta}_c/\dot{\eta}_{ns}$ with an increase in ω_T as the chamber pressure is phase shifted due to the restriction of air flux by high turbine angular velocities which would have a damping effect on the chamber hydrodynamics. Fig. 3h shows that the effect of the tide on $\dot{\eta}_c/\dot{\eta}_{ns}$ is not clear. One might expect to see an increase in $\dot{\eta}_c/\dot{\eta}_{ns}$ when the tide position is such that the plant's natural period matches the dominant wave period, but this is not seen clearly in the data. This relationship might only become clear when the incident wave period is considered simultaneously. It is also interesting to note that in almost all subplots of Fig. 3 there is an increase in $\dot{\eta}_c/\dot{\eta}_{ns}$ when the plant is non-operational. This is likely to be due to the fact that when the plant is non-operational the relief valve is always fully open so that the air pressure in the chamber is typically less than when the plant is operational and subsequently the radiation damping effect on the hydrodynamic oscillation in the chamber is lower.

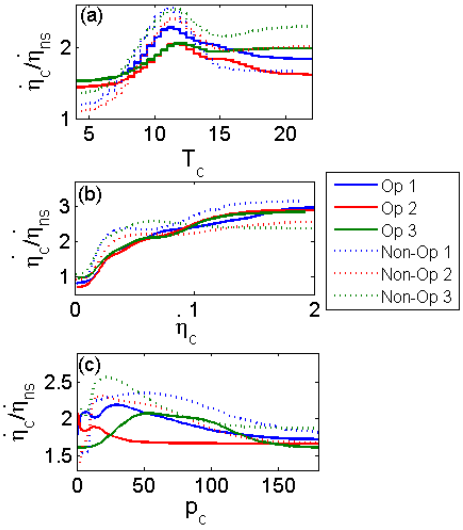

Fig. 5 Polynomial fitted curves of order 5, fitted to raw data corresponding to three Aquadopp deployment periods 1.) blue - 08/11/2010 – 21/11/2010, 2.) red - 21/11/2010 – 22/02/2011 and .3) green - 21/02/2012-22/03/2012, showing the relationship between $\dot{\eta}_c/\dot{\eta}_{ns}$ when the plant is both operational and non-operational for the following parameters that could not be used to train the ANN because they are not known in advance of the event that is being forecasted.; (a) zero-up crossing wave period (chamber), (b) the water surface vertical velocity measured (chamber), (c) the max air pressure of the wave cycle in the chamber in units of mbar.

Data from the incident wave parameters as measured in the chamber: $\dot{\eta}_c$, T_c, and p_c which is the chamber pressure, cannot be used in the forecast because they happen simultaneously or are indeed the parameter that we are forecasting. However, it is still interesting to exam the relationship with $\dot{\eta}_c/\dot{\eta}_{ns}$. Fig. 5a shows a similar profile to Fig. 3c and Fig, 3e and is somewhat in-line with the theory of the system's natural frequency except for the larger amplification of very short period waves. Fig. 5b shows an increase in $\dot{\eta}_c/\dot{\eta}_{ns}$ with an increase in $\dot{\eta}_c$. This does not appear to agree with the theory that suggests greater hydrodynamic losses occur with greater

values $\dot{\eta}_c$, and also greater damping from increased air pressure, and might be again an issue with reflected wave interference. This needs further investigation. Fig. 5c shows a decline in $\dot{\eta}_c/\dot{\eta}_{ns}$with increasing chamber pressure which is in-line with theory that states that radiation damping of the hydrodynamic oscillations increases with air pressure.

When the ANN was trained with all the available data simultaneously the extremes of the peak $\dot{\eta}_c$ envelope, were under predicted. This is problematic because these are the waves that are most likely to cause the turbine to stall. This was dealt with by separating the data into sets based on the value of $\dot{\eta}_{ns}$ with respect to the local mean $\overline{\dot{\eta}_{ns}}$ and standard deviation $\sigma_{\dot{\eta}_{ns}}$ of the preceding 1 hour of data. Data was divided in to the following sets: those less than the local mean $\dot{\eta}_{ns} < \bar{\dot{\eta}}_{ns}$, those between the local mean and the local upper standard deviation $\bar{\dot{\eta}}_{ns} < \dot{\eta}_{ns} < \bar{\dot{\eta}}_{ns} + \sigma_{\dot{\eta}_{ns}}$ and finally those above the local standard deviation $\bar{\dot{\eta}}_{ns} + \sigma_{\dot{\eta}_{ns}} < \dot{\eta}_{ns}$. A separate ANN was trained for each of the three data sets. In operation the trained ANN that is used to forecast the peak $\dot{\eta}_{c,f}$ (forecasted peak vertical water surface velocity in the chamber) will be determined on a wave by wave basis and by the parameters $\dot{\eta}_{ns}$, $\overline{\dot{\eta}_{ns}}$ and $\sigma_{\dot{\eta}_{ns}}$.

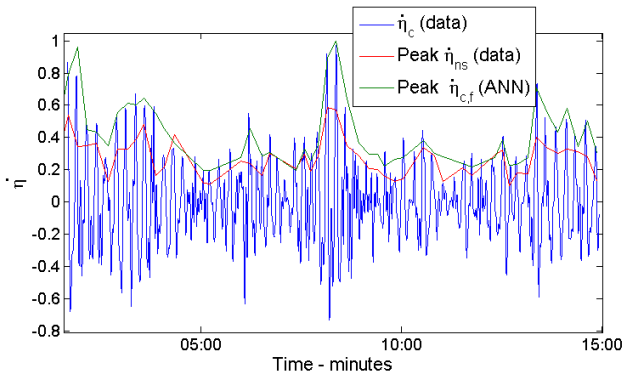

Fig. 6 Example time series of measured target water surface vertical velocity in chamber $\dot{\eta}_c$ (blue), the peak water surface vertical velocity envelope at near-shore sensor (red) and the ANN forecasted peak water surface vertical velocity envelope in the chamber $\dot{\eta}_{c,f}$ (green).

To try to quantify the accuracy of the ANN forecasted vertical water surface velocity $\dot{\eta}_{c,f}$ we evaluate the difference between $\dot{\eta}_{c,f}$ and the true $\dot{\eta}_c$for every wave cycle of the whole of the most recent Aquadopp data collection period (period 3, 21/02/2012 to 22/03/2012). A short sample operational time series of the forecasted peak $\dot{\eta}_{c,f}$ wave envelope is shown in Fig. 6.

To aid with the evaluation we define the statistical parameters:

1. ΔRaw - the difference between the unmodified vertical surface velocity at the near-shore sensor $\dot{\eta}_{ns}$ and the chamber vertical surface velocity $\dot{\eta}_c$, as a percentage of $\dot{\eta}_c$, so that $\Delta Raw = 100\%(\dot{\eta}_{ns} - \dot{\eta}_{c,})/\dot{\eta}_c$
2. ΔANN - the difference between the ANN forecasted vertical surface velocity in the chamber $\dot{\eta}_{c,f}$ and the actual chamber vertical surface velocity $\dot{\eta}_c$, as a percentage of $\dot{\eta}_c$, so that $\Delta ANN = 100\%(\dot{\eta}_{c,f} - \dot{\eta}_c)/\dot{\eta}_c$

TABLE I
% IMPROVEMENTS IN FORECASTED VERTICAL WATER SURFACE VELOCITY (CHAMBER) USING ANN COMPARED TO THE RAW VERTICAL WATER SURFACE (NEAR-SHORE).

		$\dot{\eta}_{ns}$ T_{ns}	$\dot{\eta}_{ns}$ T_{ns} $\dot{\eta}_{ns-1}$ T_{ns-1}	All
$\dot{\eta}_{ns} < \bar{\dot{\eta}}_{ns}$	ΔRaw	40.0%	40.0%	40.0%
	ΔANN	32.7%	29.4%	26.8%
$\bar{\dot{\eta}}_{ns} < \dot{\eta}_{ns}$ $\dot{\eta}_{ns} < \bar{\dot{\eta}}_{ns} + \sigma_{\dot{\eta}_{ns}}$	ΔRaw	45.9%	45.9%	45.9%
	ΔANN	19.3%	15.4%	13.3%
$\bar{\dot{\eta}}_{ns} + \sigma_{\dot{\eta}_{ns}} < \dot{\eta}_{ns}$	ΔRaw	50.7%	50.7%	50.7%
	ΔANN	18.1%	14.5%	11.7%

Table 1 shows that the ANN trained on all available variables, on average, for each wave cycle of the whole of data collection period 3, predicts the value $\dot{\eta}_c$ to between 26.8% and 11.7% of the true value. The accuracy increased with the relative local increase of $\dot{\eta}_{ns}$, with the accuracy the ANN forecasted $\dot{\eta}_{c,f}$ value peaking for waves with $\dot{\eta}_{ns}$ greater than one standard deviation greater than the mean. This is the range most relevant for stall reduction purposes. Table 1 also shows the accuracy of the ANN when trained on only the incident and preceding wave parameters measured at the near-shore sensor, and for just the incident wave parameters measured at the near-shore sensor. With the reduction in the number of variables there is a notable reduction in accuracy of the ANN forecast. However, this might be justifiable from an operation perspective due to the reduction in the reliance of the accuracy of multiple data signals and hence a reduction in the potential for error.

B. Forecast step 2 – Turbine angular velocity dependent air velocity stall threshold

As mentioned before, from monitoring it was found that the onset of a turbine stall could typically, but not infallibly, be identified by a sharp increases in the vibrations of the turbine generator structure. So a threshold value of the time derivative of the vibrations $\dot{V}$, which was found from monitoring to be $10mms^{-2}$, was used to identify when the turbine stalled in a wave cycle. In Fig. 7 it is seen that there is a large band that does not fit the trend of the rest of the data, and is clearly anomalous form the theory. This is because the 1st harmonic of the generator turbine structure is within the operational turbine angular velocity range. In this region, due to the natural frequency of the generator turbine system, vibrations are already significant so additional vibration and the associated gradient is less prominent.

Using the vibration gradient as an indicator for stall events and for determining the angular velocity dependent threshold air-velocity for stall, for use with the relief valve control algorithm, is less than ideal. For implementation into the

algorithm we were forced to interpolate through this 1st harmonic region. A more accurate method of stall detection should be considered in due course to enhance the accuracy of this forecast step.

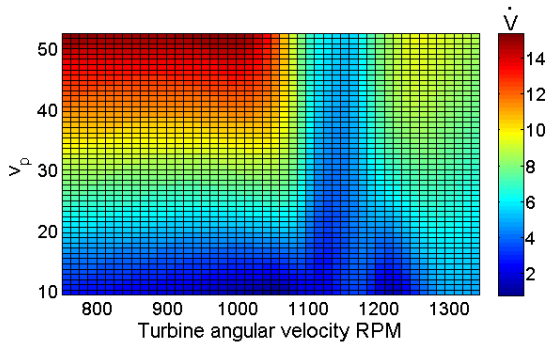

Fig. 7 Matrix 2 for identifying the maximum forecasted air-velocity that will result in a vibration gradient below the stall threshold, at a specific turbine angular velocity. A local linear regression smoothing with a span of 25% is applied to smooth and identify the main data trends.

C. *Forecast step 3 – Relief valve position*

The final forecast step required by the relief valve control algorithm for full functionality is the forecast of the relief valve aperture that will provide the airflow velocity v_p, to the turbine, without breaching the turbine's angular velocity dependent threshold for stall, as described in forecast step 2, from the forecasted value of $\dot{\eta}_{c,f}$ from forecast step 1. Fortunately there is approximately two weeks' of operational data where the relief valve position was recorded, and although this was insufficient to be included in the ANN forecast of $\dot{\eta}_{c,f}$, it was sufficient to construct the matrix for forecasting the peak air flow velocity v_p from the peak $\dot{\eta}_c$ and the relief valve position, because the trends are so clear. This is shown in Fig. 8.

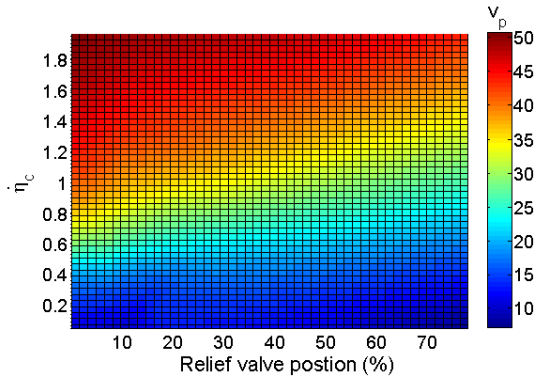

Fig. 8 Matrix 3 for forecasting the relief valve position that will provide the maximum air velocity of exhale cycle (determined in matrix 2) from the maximum vertical water surface velocity of wave cycle in the chamber (forecasted by matrix 1). A local linear regression smoothing with a span of 25% is applied to smooth and identify the main data trends.

D. *Control algorithm*

A simple description of the algorithm's architecture is shown in Fig. 9. The algorithm will act immediately as $\dot{\eta}_{ns}$ (the last variable to be known in time) is measured. This is entered into a data vector containing the other 7 operational parameters that have been identified to be significant in determining $\dot{\eta}_{c,f}$. The data vector is used to quarry one of the pre-trained ANNs, depending on its relative magnitude with respect to the local means and standard deviation as described in Table 1, to forecast the vertical water surface velocity in the chamber $\dot{\eta}_{c,f}$. The algorithm will have information on the current turbine angular velocity and will use a look-up table to find the air-velocity threshold for stall $v_{p,f}$, as described in step 2. The forecasted values of $\dot{\eta}_{c,f}$ and $v_{p,f}$ will then be entered into a final look-up table to forecast the relief valve position that will result in the target value of $v_{p,f}$, from the peak of the incident wave cycle. The algorithm will then actuate the relief valve and attempt to achieve this forecasted position. This will repeat when the next zero up crossing occurs at the near-shore sensor.

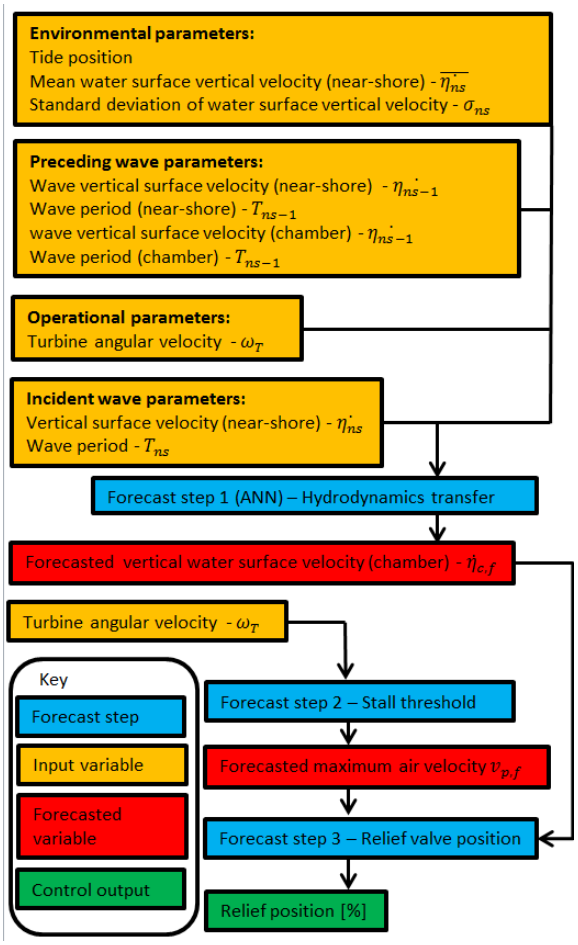

Fig. 9 Flow chart showing the relief valve control algorithm process chain

III. Discussion

The forecast chain relating near-shore hydrodynamics to optimum relief valve position was formed of three separate steps. This was necessary because the data from all the required parameters were not available simultaneously, due to the addition of different sensors at different times. If they

were available simultaneously an ANN to forecast the whole chain in one step, might have been possible. This might reveal some other interdependencies between the forecast steps and will be assessed when data becomes available in the future.

Comparing our results to the literature suggest that the limitations in the accuracy of the ANN's forecast are likely to be the result of reflected waves interfering with incident wave data at the near-shore sensor. In addition the lack of data on the relief valve position (and its omission from the training of the ANN) will result in the ANN being, in part, "blind" to the effects of damping from the compression of air, and which may also limit the accuracy of the ANN. Deploying a sensor system that can extract the incident wave from the reflected wave, and by including the forecasted chamber pressures will likely improve the forecast accuracy of $\dot{\eta}_{c,f}$.

The forecast and control system developed here accounts for and is restricted by the limitations associated with the slow aperture adjustment rate of the actual relief valve installed at the Pico OWC. It is unlikely to achieve the enhancement to power production that might be achievable with a fast acting relief valve that can track the full pressure evolution of the complete wave cycle. This is because some pneumatic power from all but the peak portion of the cycle will be lost to the atmosphere. However, any significant success achieved with this system will strongly justify the investment required to install a faster acting relief valve.

IV. Conclusions

We disseminate for first time an existing system for real-time relief valve control that has been used successful in real-time operation at the Pico OWC. However, the main feature of this research is the subsequent advancement of this relief-valve control system. This was achieved by considering many additional variables that theoretically influence the transfer of incident wave hydrodynamics to the eventual mechanical response. Forecast models were made directly from data and, in one case, with the assistance of artificial neural networks, to more accurately forecast the optimum relief valve position for the incident waves.

The greatest accuracy in the forecasted chamber hydrodynamics was achieved when the ANN was provided with as many relevant operational, environmental, incident and preceding wave parameters as possible. Some reduction in accuracy in the forecast occurs when just the incident wave parameters and the preceding wave parameters at the near-shore sensor are provided to the ANN. This reduction in accuracy might be justifiable in practical operation because of the reduction in the potential for error.

Clear trends were seen in the data that agree somewhat with theory and the literature. In most instances departure of our results from theory can be explained by interference from reflected waves at the near-shore sensor. However, three points need further attention, these are: the absence of data on the relief valve position which could significantly affect the forecast due to the radiation damped effect from air compression in the chamber, the interference of measurements by the near-shore sensor due to wave reflections, the non-definitive, vibration gradient method, used for stall detection.

References

[1] A.F. de O. Falcao, "The shoreline OWC Wave Power Plant at the Azores", in: *Proc EWTEC*, 2000, pp.42-48.

[2] A.F. de O. Falcao, "Control of an oscillating-water-column wave power plant for maximum energy production", *Applied Ocean Reserch*, Vol. 24, pp. 73–82, 2002.

[3] M. Alderbi, M. Amundarain, A. J. Garrido, I. Garrido, O. Casquero, and M. De la sen. "Complementary Control of Oscillating Water Column-Based Wave Energy Conversion Plants to Improve the Instantaneous Power Output", *IEEE Transactions on Energy Conversion*, Vol. 26, pp. 1021-1032, 2011.

[4] A.F. de O. Falcao, L. C. Vieira, P. A. P. Justino, J. M. C. S. Andre, "By-pass air-valve control of an OWC Wave power plant", *Offshore mechanics and arctic engineering*, Vol. 125, pp. 205–210, 2003.

[5] F. Fusco, J. V. Ringwood, "Short term wave forecasting with AR models in real-time optimal control of wave energy converters", *IEEE Transactions on sustainable energy*, 2010, pp. 99-106.

[6] B. Fischer, P. Kracht, and S. Perez-Becker, "Online-Algorithm using Adaptive Filters for Short-Term Wave Prediction and its Implementation", in: *Proc ICOE*, 2012

[7] J. Tedd and P. Frigaard, "Short term wave forecasting, using digital filters, for improved control of Wave Energy Converters", in: *Proc ISOPE*, 2007, pp. 388-394

[8] F. Ferri, M. T. Sichani and P. Frigaard, "A Case Study of Short-term Wave Forecasting Based on FIR Filter: Optimization of the Power Production for the Wavestar Device", in: *Proc ISOPE*, 2012, pp. 628-635

[9] J. Dannenberg, K. Hessner, P. Naaijen, H. van den Boom and K. Reichert, "The On Board Wave and Motion Estimator OWME",in: *Proc ISOPE*, 2010, pp. 424-431

[10] D. V. Evans and R. Porter, "Hydrodynamic characteristics of an oscillating water column device," *Applied Ocean Research*, Vol. 17, pp. 155-164, 1995.

[11] R. V. Veer and H. J. Thorlen, "Added resistance of moonpool in calm water," in: *Proc ASME*, 2008.

[12] I. Morrison and C. Greated, "Oscillating water column modelling," in: Proc. *ICCE*, 1992 pp. 502.

[13] Zhang, Y.L., **Q.-P. Zou**, & D. Greaves: "An investigation of hydrodynamic characteristics of an oscillating water column device using a two-phase flow model," *Renewable Energy*, Vol. 41, pp. 159–170, 2012.

[14] M. T. Morris-Thomas, R. J. Irvin, R. J. and K.P Thiagarajan, "An Investigation into the hydrodynamic efficiency of an oscillating water column," *Journal of Offshore Mechanics*, 129(4), pp. 273-278, 2007.

[15] Y. M. C. Delaur and A. Lewis, "A 3D Parametric Study of a Rectangular Bottom-Mounted OWC Power Plant," in. *Proc; ISOPE*, 2001, pp. 548.

[16] M. Folley and T. Whittaker, "The effect of plenum chamber volume and air turbine hysteresis on the optimal performance of oscillating water columns," in: *Proc OMAE*, 2005.

[17] M. Alves, M. Vicente, A. J. N. A. Sarmento, and M. Guerinel, "Implementation and Verification of a Time Domain Model to Simulate the Dynamics of OWCs," in: *Proc EWTEC*, 2011.

[18] M. Folley and T. Whittaker, "Validating a spectral-domain model of an OWC using physical model data," in: *Proc EWTEC*, 2011.